

Performance Characteristics and Energy Loss Analyses of a High-Speed Centrifugal Pump with Straight Blades

X. Su¹, W. Jin¹, Z. Zu¹, Z. Li² and H. Jia^{1†}

¹ National-Provincial Joint Engineering Laboratory for Fluid Transmission System, Zhejiang Sci-Tech University, Hangzhou 310018, China

² Changsha Research Institute of Mining and Metallurgy, Changsha 410012, China

†Corresponding Author Email: jiahao@zstu.edu.cn

Received October 20, 2020; accepted March 19, 2021)

ABSTRACT

Along with the rapid growth of cutting-edge petrochemical technology and the pressing demand for efficiency improvement, evaluation of the performance characteristics of high-speed pump is becoming increasingly important. In this paper, numerical simulation is presented on the flow instability of a 16 straight-blade high-speed centrifugal pump with flow rate of 3 m³/h and rotating speed of 8500 rpm. Combined with the analysis of flow stability, the entropy production method is introduced to evaluate regions of high mechanical energy loss and its distribution at different flow rates. Results show that approximately 96% of the energy loss of the pump is produced in the volute, gap, and front and back chambers. Large energy loss is observed near the trailing edge of the blade and volute tongue, which are caused by the small region including both the high and low pressure gradients and large momentum exchange by the flow separation, respectively. Moreover, the rotor–stator interaction causes much energy loss at the wall of the volute and front and back chambers. Owing to the circumferential pressure gradient and the 90° leading edge of the straight blade, the fluid tends to form counter-rotating recirculation vortices. The large number of blades narrows the passage and limits the formation of large vortices in flow channels, thus the backflow phenomenon seems not to worsen with the rise of flow rates. Hence, the entropy production in most of the flow parts are insensitive to flow rates.

Keywords: High-speed centrifugal pump; Entropy production; Straight blade; Flow stability; Energy loss.

NOMENCLATURE

Q	flow rate	$S_{pro,D'}$	entropy production by velocity fluctuation
Q_d	design flow rate	T	temperature
S_D	entropy production rate	$\bar{u}, \bar{v}, \bar{w}$	time averaged velocity
$S_{\bar{D}}$	entropy production rate induced by time averaged movement	u', v', w'	pulsating velocity
$S_{D'}$	entropy production rate by velocity fluctuation	μ	viscosity
S_{pro}	entropy production	μ_t	turbulent dynamic viscosity
$S_{pro,\bar{D}}$	entropy production induced by time-averaged movement	μ_{eff}	effective viscosity
		y^+	dimensionless wall distance

1. INTRODUCTION

High-speed centrifugal pumps have been widely used in situations where high head are needed for relatively low flow rate, such as aero-engine, petrochemical, and oil refining equipment. Compared with those in a normal-speed pump, the energy density of per unit fluid volume is higher, thus a small disturbance or flow instability could cause performance drop or fluctuation of service. Thus,

weakening the effect of turbulence and unsteady flow in the passage to a certain degree is helpful but rather difficult. In common sense, it is considered weak connection between the behavior of efficiency and flow stability, but a closer link between the two issues always appears in the flow of high-speed pump. Along with the rapid growth of cutting-edge petrochemical technology, it is very important to reduce the hydraulic loss and improve the operating efficiency of high-speed pump by evaluating its

unstable flow characteristics (Jia *et al.* 2018; Li Y. *et al.* 2017; Yuan and Yuan 2017).

In recent years, CFD (computational fluid dynamics) method is more and more adopted to research high-speed pump. Jafarzadeh *et al.* (2011) numerically studied a pump with rotation of over 13,000 rpm and found the influence of blade number and position of leading and trailing edge on the hydraulic loss and flow characteristics. Alemi *et al.* (2015) researched the design method of high-speed pump volute and its corresponding performance, and found that a hydraulic combination of volute and radial diffuser could promote the behavior of the efficiency and radial force balance. Yang *et al.* (2019) took a full-scale oxygen pump (18,000 rpm) of a liquid rocket engine as object, explored the rotor clocking effect, and found an approximately 1.5% difference on efficiency when the rotor and stator were at different circumferential positions. Cui *et al.* (2018) studied the transient cavitating characteristics in a high-speed pump and discussed the development of the bubbles and the cavitation instabilities.

The common method for exploring the hydraulic loss mostly concentrates on the pressure drop, which is limited by not knowing the exact location of high energy loss. Recently, many researchers have reported that losses due to turbulence flow and friction that are often attributed to efficiency drop are closely related to local entropy production rate (Chang *et al.* 2019; Li Y. *et al.* 2017; Yang *et al.* 2019). Pei *et al.* (2016) studied the effect of the distance on the whole power loss and the spatial flow-loss distribution by using the entropy generation method in a pump with low head, and they concluded that the turbulence dissipation dominates the energy loss. Yang *et al.* (2019) evaluated the hydraulic loss produced in a pump by presenting a corrected entropy production method involving the wall effects. Hou *et al.* (2017) found that turbulent fluctuation and wall friction are the main factors in affecting irreversible hydraulic loss in a centrifugal pump. Wang *et al.* (2019) proposed an entropy generation diagnostic model involving the contribution of turbulent entropy generation, viscous entropy generation and wall entropy generation for the analysis of cavitation flow in a two-stage pump. They discovered that the rapid growth of the loss in guide vane and impeller of the second-stage dominates energy loss after cavitation.

The influence of structural parameters of blade on high-speed pump performance have been investigated by analyzing the flow characteristics and entropy production. The design of splitter blade has been confirmed to enhance the flow uniformity and minimize the occurrence of cavitation (DAVID 1997). Principles of the design of splitter blade have been investigated, including blade number, inlet diameter of blade passage, and deflection angle of blade (Yuan *et al.* 2009; Yuan and Yuan 2017). Yuan concluded that the splitter blade improves the flow stability by decreasing the dissipation of turbulent kinetic energy (Yuan and Yuan 2017).

Different from that of the splitter blade, the design of straight blade (not twisted, angle of trailing edge

nearly 90°) can produce high head of the high-speed pump with less modification of the pump structure (Song *et al.* 2010). In small-scale pumps, manufacturing the impeller with straight blades is much easier and more cost-efficient than those with spiral-profile blades (Fang *et al.* 2020). Given such characteristics, straight-blade pump fits in the applications requesting small flowrate as well as high head (Cui *et al.* 2013). However, strong flow separations may take place at the suction side in the entrance of blade channel which could cause strong circulating flow in the passages unlike the spiral-profile blades (Song *et al.* 2010). Hence, pumps with straight blades often suffer low efficiency. In addition, the rotor-stator interaction between the rotational straight impeller and stationary volute can cause strong unsteady flow fields. Unfortunately, few studies of hydraulic performance and entropy production research high-speed centrifugal pumps with straight blade.

This paper investigates numerically the flow characteristic of a high-speed centrifugal pump with a rotation speed of 8500 rpm. Numerical simulation was performed using the commercial software ANSYS-CFX, and the model was validated by the experimental data. The entropy production method was employed to analyze the energy loss of the main flow passages of the pump. The results obtained from different flow rates clearly show the rotor-stator interaction between the rotating impeller and stationary volute and front and back chambers. The reason of energy loss was determined through a comprehensive analysis of the entropy production and flow characteristics.

2. METHODS

2.1 Entropy Production Theory

Flow in centrifugal pump will inevitably result in energy loss, which can be reflected by the rate of entropy production. The flow loss is due to the existence of viscosity and Reynolds stress, which leads to irreversible dissipation effect. Given that most turbomachines are closely adiabatic, entropy production contributes significantly to the loss of efficiency owing to irreversible processes. In addition, the unsteady phenomenon, such as vortex in the flow field, will aggravate the flow loss, that is, the entropy production will increase. For Reynolds time averaged turbulence, the local entropy production rate (LEPR) is mainly composed of two parts. One is caused by time-averaged movement, and the other is caused by fluctuating movement. The LEPR can be calculated by the following formula (Li D. *et al.* 2017)

$$S = S_{\bar{D}} + S_{D'} \quad (1)$$

The LEPR induced by time averaged velocity can be calculated as (Li D. *et al.* 2017)

$$S_{\bar{D}} = \frac{\mu}{T} \left[\left(\frac{\partial \bar{u}}{\partial y} + \frac{\partial \bar{v}}{\partial x} \right)^2 + \left(\frac{\partial \bar{u}}{\partial z} + \frac{\partial \bar{w}}{\partial x} \right)^2 + \left(\frac{\partial \bar{w}}{\partial y} + \frac{\partial \bar{v}}{\partial z} \right)^2 \right]$$

$$+ \frac{2\mu}{T} \left[\left(\frac{\partial \bar{u}}{\partial x} \right)^2 + \left(\frac{\partial \bar{v}}{\partial y} \right)^2 + \left(\frac{\partial \bar{w}}{\partial z} \right)^2 \right] \quad (2)$$

The LEPR induced by the fluctuation velocity is expressed as (Li D. *et al.* 2017)

$$S_{D'} = \frac{\mu_{eff}}{T} \left[\left(\frac{\partial u'}{\partial y} + \frac{\partial v'}{\partial x} \right)^2 + \left(\frac{\partial u'}{\partial z} + \frac{\partial w'}{\partial x} \right)^2 + \left(\frac{\partial w'}{\partial y} + \frac{\partial v'}{\partial z} \right)^2 \right] + \frac{2\mu_{eff}}{T} \left[\left(\frac{\partial u'}{\partial x} \right)^2 + \left(\frac{\partial v'}{\partial y} \right)^2 + \left(\frac{\partial w'}{\partial z} \right)^2 \right] \quad (3)$$

where μ_{eff} is the effective dynamic viscosity, which is expressed as

$$\mu_{eff} = \mu + \mu_f \quad (4)$$

The time-averaged term $S_{\bar{D}}$ can be calculated directly from a RANS equation, but the fluctuating term $S_{D'}$, which cannot be determined as the component of velocity fluctuation, is unavailable in RANS simulation (Li D. *et al.* 2017). Based on the theory proposed by Kock (Kock and Herwig 2004) and Mathieu (Mathieu and Scott 2000), the difference between $\rho\varepsilon$ and the turbulent dissipation is asymptotically small and disappears when Reynolds number tends to the positive infinity. Therefore, in the $k-\varepsilon$ turbulent model, $S_{D'}$ is given as

$$S_{D'} = \frac{\rho\varepsilon}{T} \quad (1)$$

The entropy production rate could be obtained through volume integration of LEPR. The respective expressions are as follows

$$S_{pro,\bar{D}} = \int_V S_{\bar{D}} dV \quad (2)$$

$$S_{pro,D'} = \int_V S_{D'} dV \quad (3)$$

The overall entropy production can be calculated as

$$S_{pro} = S_{pro,\bar{D}} + S_{pro,D'} \quad (4)$$

2.2 Physical Model

The high-speed pump with the rotating speed of 8500 r/min was adopted as the model pump with its designed flow rate and total head of 3 m³/h and 250 m, respectively. The computational domain includes seven parts: inlet duct, inducer, front chamber, impeller, gap, volute, and back chamber (Fig. 1). The inlet and outlet tubes are both extended to minimize the effect of boundary conditions on the main flow field. Detailed structural parameters are shown in Table 1.

2.3 Grid Generation and Numerical Settings

The mixed grids of hexahedron and tetrahedron were generated to fit the different region of the computational domain. The grid of rotating domains of inducer and impeller are shown in Fig. 2.

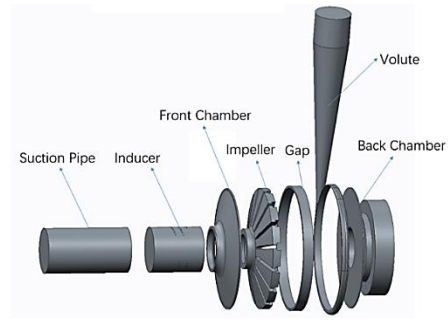
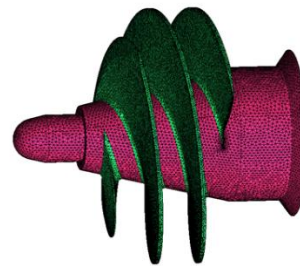


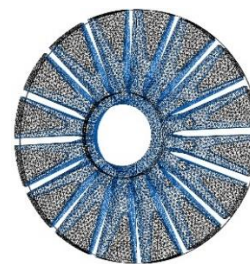
Fig. 1. Computational domain.

Table 1 Basic parameters of the pump.

Parameters	Value
Inlet diameter/mm	50.0
Outlet diameter/mm	40.0
Impeller outlet diameter/mm	132.0
Number of blades	16
Impeller outlet width/mm	27.2
Pitch of inducer/mm	8.6
Length of inducer/mm	57.3
Leading/Trilling edge angle/°	90
Inducer wrap angle/°	439.5
Base circle diameter of volute/mm	68.5
Phase angle of volute tongue/°	14.1
Specific Speed	3.9



(a)



(b)

Fig. 2(a, b). Computational meshes of the inducer and impeller.

Four sets of grids were adopted to verify the independence of the number of grids based on the steady simulation at flow rates of 0.2 Q_d . Figure 3 shows the effect of grid size when chosen head as an indicator. The difference of head falls below 1% when the grid number exceeds 4.0 million. Therefore, 4.17 million grid number was used in the

simulations. The grids near wall surface is specially treated, Fig. 4 displays y^+ values on the wall with the maximum below 150, indicating the choice of scalable wall function is reasonable.

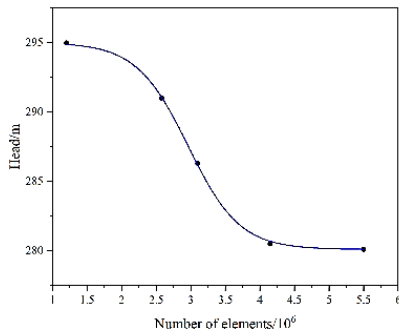


Fig. 3. Grid dependence validation.

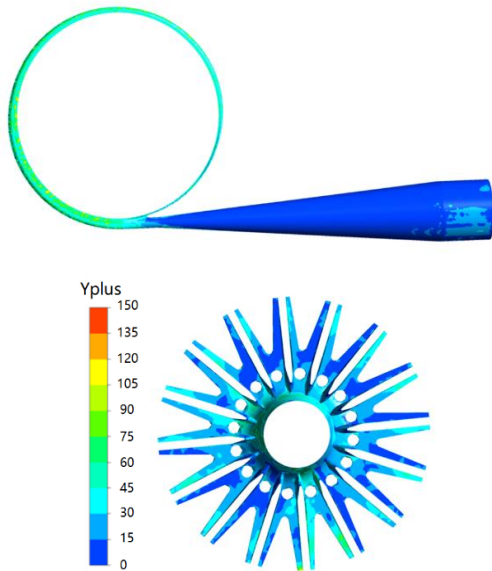


Fig. 4. y^+ appearance

ANSYS CFX was adopted to perform the simulation. The realizable $k-\epsilon$ model was used to simulate the

incompressible steady flow in the pump due to its good accuracy and relative low calculation cost. The velocity inlet and pressure outlet condition were adopted at the inlet and outlet boundaries, respectively. No-slip wall condition was set for all the walls. The convergence residual was set as 10^{-5} . The well-known SIMPLEC algorithm was used to deal with velocity–pressure coupling. The steady simulations were performed under different operating conditions, with multiple reference frame (MRF) approach.

2.4 Experiment Validation

The hydraulic performance test of the model pump was conducted at the National-Provincial Joint Engineering Laboratory for Fluid Transmission System, Zhejiang Sci-Tech University. The testing apparatus was mainly composed of a tested pump, two pressure transmitters, a flowmeter, and some pipelines and regulating valves, as shown in Fig. 5. The inlet pipeline connects with the bottom of the water tank with a volume of $3 \text{ m}^3/\text{h}$, and the outlet pipeline returns to the top of the water tank. The experimental setup was available for performance assessment of high-speed pumps within an uncertainty of 0.3%-0.5% in an open loop. The working fluid was room-temperature water. The pump inlet and outlet pressures were measured by pressure gauges with the accuracy of 0.25%. The flow rates were measured by an electromagnetic flowmeter with the uncertainty of 0.2%. The first-order uncertainty analysis was calculated by the method to calculate the combined uncertainty (Su *et al.* 2016; Su *et al.* 2020). The uncertainty of flow rate, head, efficiency and power is $\pm 0.55\%$, $\pm 0.895\%$, $\pm 1.421\%$ and $\pm 0.956\%$, respectively. The uncertainty mentioned above is not a function of measured quantity and these uncertainties apply to all data points.

Figure 6 shows the comparison between experiments and numerical simulation on the different values of flow rates. The relative error of most of the tested points is less than 5%. Therefore, the numerical simulation is reliable. The simulation results are a little larger than those of the experiment because the mechanical loss and seal loss were not considered in the numerical model.

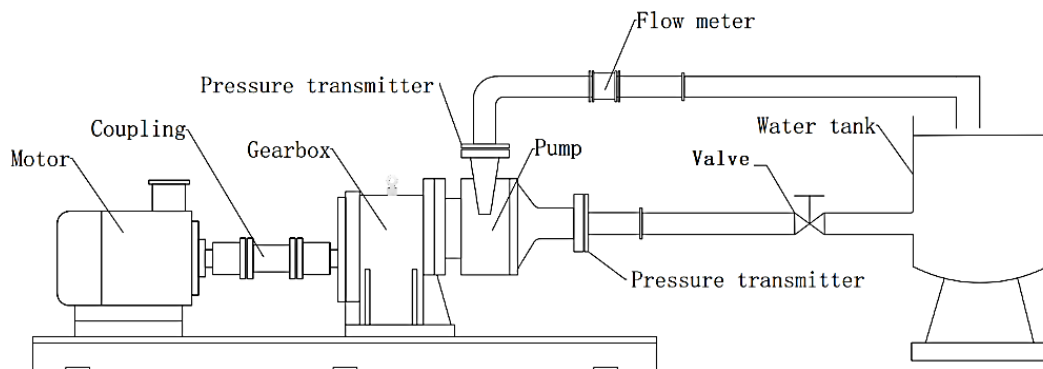


Fig. 5. Schematic of experimental apparatus.

The head drops gently with the increase of flow, whereas the efficiency increases drastic with the increase of flow. The head drops approximately 30 m as flow rates increase from $0.2 Q_b$ to $1.4 Q_b$, whereas the efficiency increases from 2.5% to 20%. Low efficiency of the pump means particular flow characteristic and energy loss in the operation of the pump, which is analyzed in the following section.

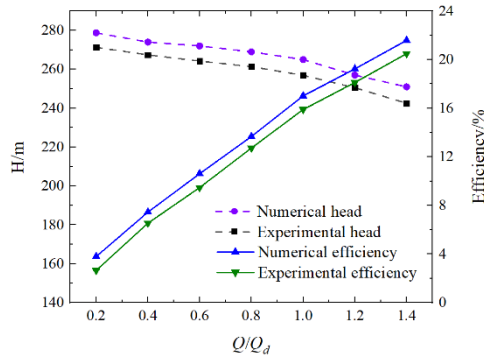


Fig. 6. Comparison of the head and efficiency between experiment and simulation.

3. RESULTS AND DISCUSSION

3.1 Flow Characteristics

The flow feature is exposed in this section for four different conditions (20%, 60%, 100%, and 140% of the designed flow rate) to study the differences among these operating points.

The dimensionless pressure is defined as follows:

$$P^* = \frac{P - P_{inlet}}{0.5 \rho v_u^2} \quad (9)$$

Where P is the static pressure, P_{inlet} is the static pressure at the inlet, ρ is the fluid density, and v_u is the circumferential velocity at the outer edge of the impeller

The dimensionless velocity is defined as follows:

$$V^* = \frac{v}{v_u} \quad (10)$$

Furthermore, the dimensionless pressure gradient is defined as $\frac{\partial P}{\partial L} = \frac{\Delta P^*}{R}$, where R is the radius of rotor.

The static pressure fields in the impeller at $0.2 Q_d$ are displayed in Fig. 7. With the rotation of the impeller, the pressure of the fluid in the flow passage increases continuously from the impeller inlet to the outlet. At the same radial position of the impeller, the pressure on the pressure surface of the blade is lower than that on the suction surface. With the increase of flow rates, high pressure region at the outlet increases, but the overall trend remains unchanged (not shown). Different from the symmetrical structure of impeller, the asymmetry of volute leads to the complex structure of pressure distribution at the near-tongue region and related passage of impeller (Fig. 7). The pressure is further increased due to the diffuser

structure of the volute.

To show clearly the characteristics in different flow conditions, the pressure gradient is shown in Fig. 8. A small region, including high and low pressure gradients, dispersedly distributes in the gap at the trailing edge of the blade in all flow rates (see the enlarged part). The region marked in Fig. 8 among different flow rates are enlarged and shown in Fig. 9. The high pressure gradient area (red region) decreases with the increase of flow rate. The low pressure gradient region in the impeller adjacent to the tongue almost disappears at $1.0 Q_d$ and $1.4 Q_d$.

When analyzing the streamlines in Fig. 10, the flow is noted in bad guidance along the impeller passages. Owing to 90° leading edge of the straight blade and the pressure difference between the pressure and suction surface, the radial entering fluid mix with the circumferential sliding fluid, and then forms recirculation vortex. The internal displacement flow superposed upon the normal flow, forming recirculation vortex with counter rotation (Barrio *et al.* 2010).

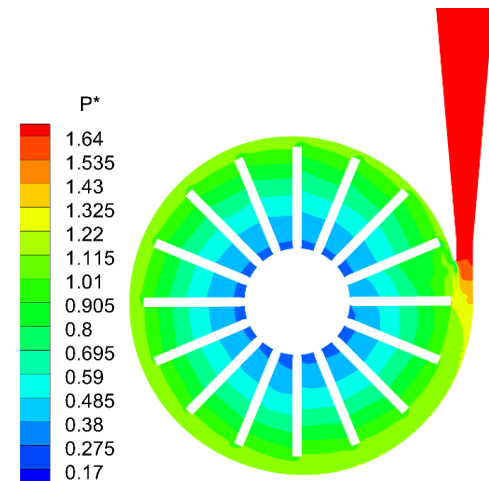


Fig. 7. Distribution of static pressure in the central section of impeller under different flow rates at $0.2 Q_d$.

High relative velocity is acquired at the external side of the counter-rotating vortex, especially in the channel adjacent to the near-tongue region at low flow rates (Figs. 10a and b). The 16-blade pump has a narrow distance between the adjacent blades, which limits the formation of large vortices in some channels (Fig. 10). High rotation speed and the impeller with straight blades dominate the formation of the vortices in certain channels, which do not decrease with the increase of the flow rates. The largest vortex appears at the passage of two channels away from the tongue (marked as channel III). Back flow dominates channels I and II. Figure 11 shows the streamline in channel I. The absolute velocity at the near-tongue region is further investigated to explore the reason for the back flow.

Figure 12 shows the streamline of the absolute velocity near the tongue region. At the flow rate of $0.2 Q_b$, a counter-rotating vortex is located in the gap near the tongue. At the near-tongue region,

streamlines come from the lateral side (broad region) of the volute (marked with circle), pass through the impeller–tongue gap, and continue a circular movement along the medial side of the volute (narrow region). Hence, the stagnation point on the tongue is situated at the side of the exit diffuser, whereas flow separation takes place from the wall of the tongue toward the volute medial side. Owing to the high-speed rotation, the fluid flows along radial direction mixes with that sliding in the circumferential direction, then a large area of clockwise vortex occurs at the lateral side of volute

(Fig. 12a), which leads to higher relative velocity in the vortex in channel I of the impeller (red streamline in Fig. 10a). The flow separation at the near-tongue region decreases with the increase of the flow rates, represented as less vortices. At the flow rate of $1.4 Q_d$, the flow progresses even around the tongue, with a stagnation point right located at the tongue tip with no sign of flow separation. Less flow enters into the gap, weakening the formation of the vortex in the impeller passage near the tongue (Fig. 10d, no red streamline in channel I).

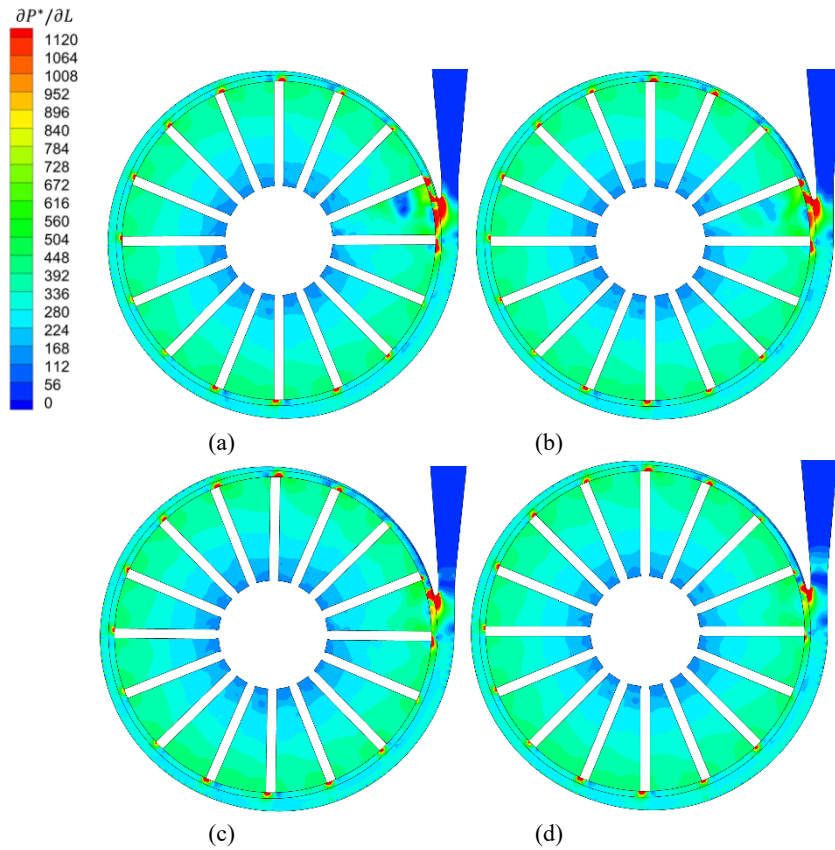


Fig. 8 (a, b, c, d). Distributions of pressure gradient at (a) $0.2 Q_d$ (b) $0.6 Q_d$ (c) $1.0 Q_d$ and (d) $1.4 Q_d$.

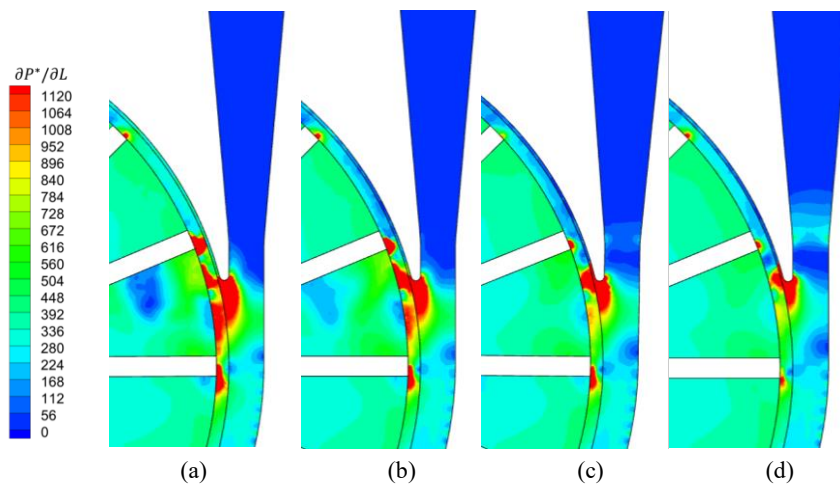


Fig. 9 (a, b, c, d). Distributions of pressure gradient at the near-tongue region at (a) $0.2 Q_d$ (b) $0.6 Q_d$ (c) $1.0 Q_d$ and (d) $1.4 Q_d$.

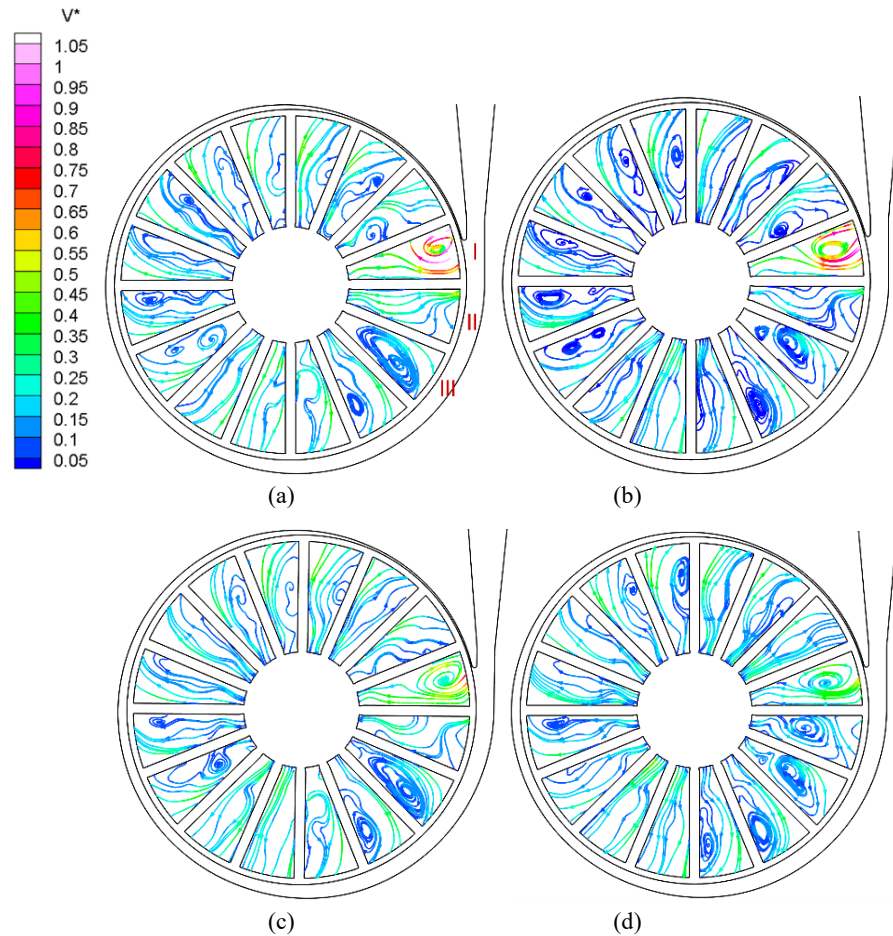


Fig. 10 (a, b, c, d). Distribution of streamlines of relative velocity in the central section of impeller under different flow rates at (a) $0.2 Q_d$ (b) $0.6 Q_d$ (c) $1.0 Q_d$ and (d) $1.4 Q_d$.

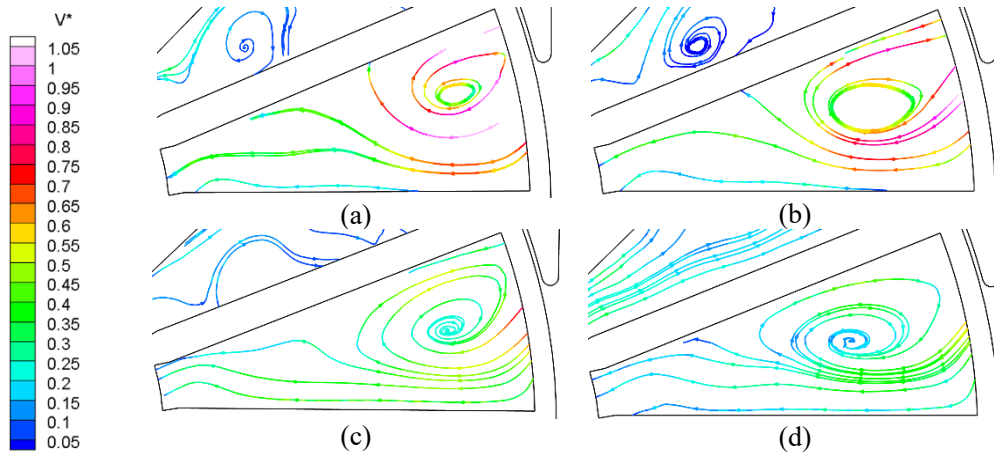


Fig. 11 (a, b, c, d). Streamlines of relative velocity in the central section of passage connect to the volute (channel I as shown in Fig. 10) at (a) $0.2 Q_d$ (b) $0.6 Q_d$ (c) $1.0 Q_d$ and (d) $1.4 Q_d$.

3.2 Entropy Production Analysis

To understand the overall energy loss of the high-speed pump, the entropic generation of each overflow component was compared. Figure 13 shows the entropy production S_{pro} under different flow rates. Most of the S_{pro} (approximately 96%) is produced in the front and back chambers, gap, and

volute. Comparatively, the S_{pro} of the impeller, inducer, and inlet pipe are far smaller and can be neglected. Entropy production in most of the flow parts are insensitive to the flow rates, whereas the S_{pro} of the volute increases smoothly with the increase of flow rate. In the following section, our analysis concentrates on the four main parts with the large S_{pro} .

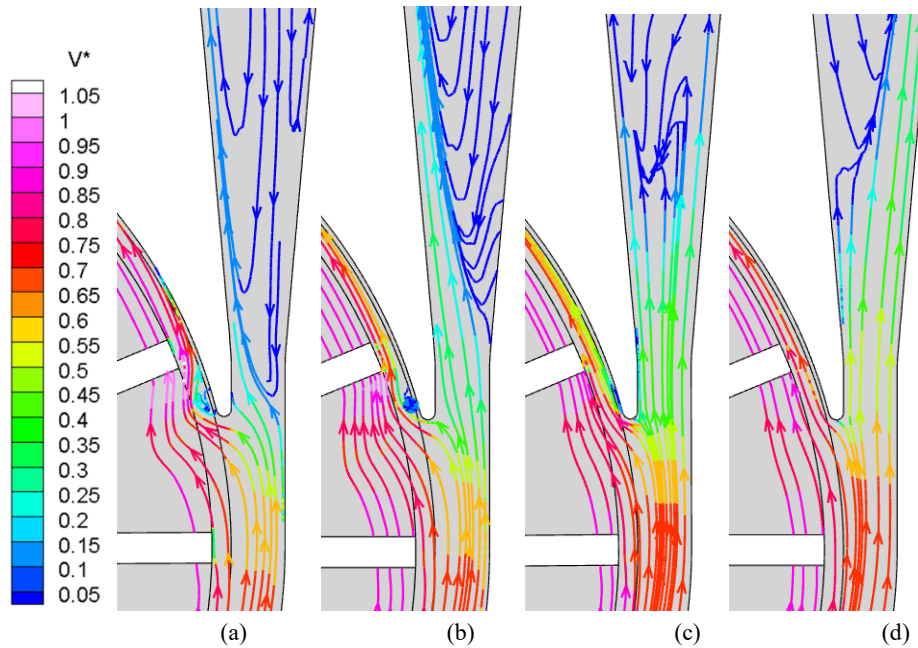


Fig. 12 (a, b, c, d). Distribution of streamlines of absolute velocity in the central section of impeller under different flow rates at (a) $0.2 Q_d$ (b) $0.6 Q_d$ (c) $1.0 Q_d$ and (d) $1.4 Q_d$.

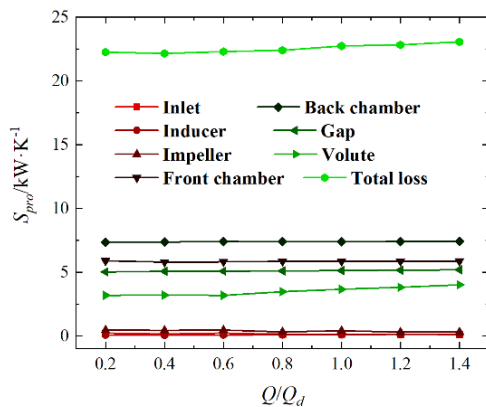


Fig. 13. Entropy production ratio versus flow rate.

3.2.1 Distribution of Entropy Production in Gap and Volute

In this section, the distribution of LEPR in gap and volute are presented to study the energy loss. Figure 14 shows the contour plot of LEPR in the volute, gap, and impeller at the four operating conditions. The high LEPR region in the gap mainly concentrates at the trailing edge of the impeller, which is consistent with the small region including high and low pressure gradients (Fig. 8). Thus, the high entropy production of the gap is caused by the circumferential fluctuation of pressure. In addition, large energy loss is observed at the gap area between channel I and the volute tongue. In this area, large momentum exchange occurs by the flow separation at low flow rates, giving rise to the relatively high energy loss (Fig. 14a). Comparing with Fig. 8, we can see the high pressure gradients at the tongue causes additional entropy production in the volute

and channel I. Combined with the flow characteristics, the relative movement of impeller rotating with respect to the volute generates unsteady interaction, which induces the flow instabilities and energy loss.

In the volute, the circumferential pressure variation (Fig. 7) causes high LEPR at the wall of the volute. From Figs. 12 and 14, the high entropy production does not appear at the large reflux region at the diffuser of the volute for the flow rate of $0.2 Q_d$ but at the friction region between the outflow and reflow. With the increase of the flow rate, the pipe is occupied by more outflow, giving rise to more friction and energy loss. By contrast, the high LEPR region in the diffuser changes from the inner wall to the out wall (Fig. 14). As shown in Fig. 15, entropy production in the diffuser increases from 0.5% to 7%, contributing to the total increase of S_{pro} in volute (see Fig. 13).

3.2.2 Distribution of Entropy Production in the Front and Back Chamber

To understand energy loss in the front and back chambers, flow in channels I and IV are shown by dividing a section according to the radius direction of the channel (as shown in Fig. 16). Figures 17 and 18 show the entropic generation and streamline distribution at different flow rates in channels I and IV, respectively. Figures 17 and 18 indicate that S_{pro} is higher at the position of larger radius in the front or back chamber. Figure 10 illustrates that the flow separation and recirculation vortex become more severe and finally occupy some passages along the radius of the impeller. Therefore, higher loss is generated because of the more complex pattern of unstable flow in the impeller channel at the shroud. Peak values of entropy production seem to occur very close to the wall of the front and back chambers,

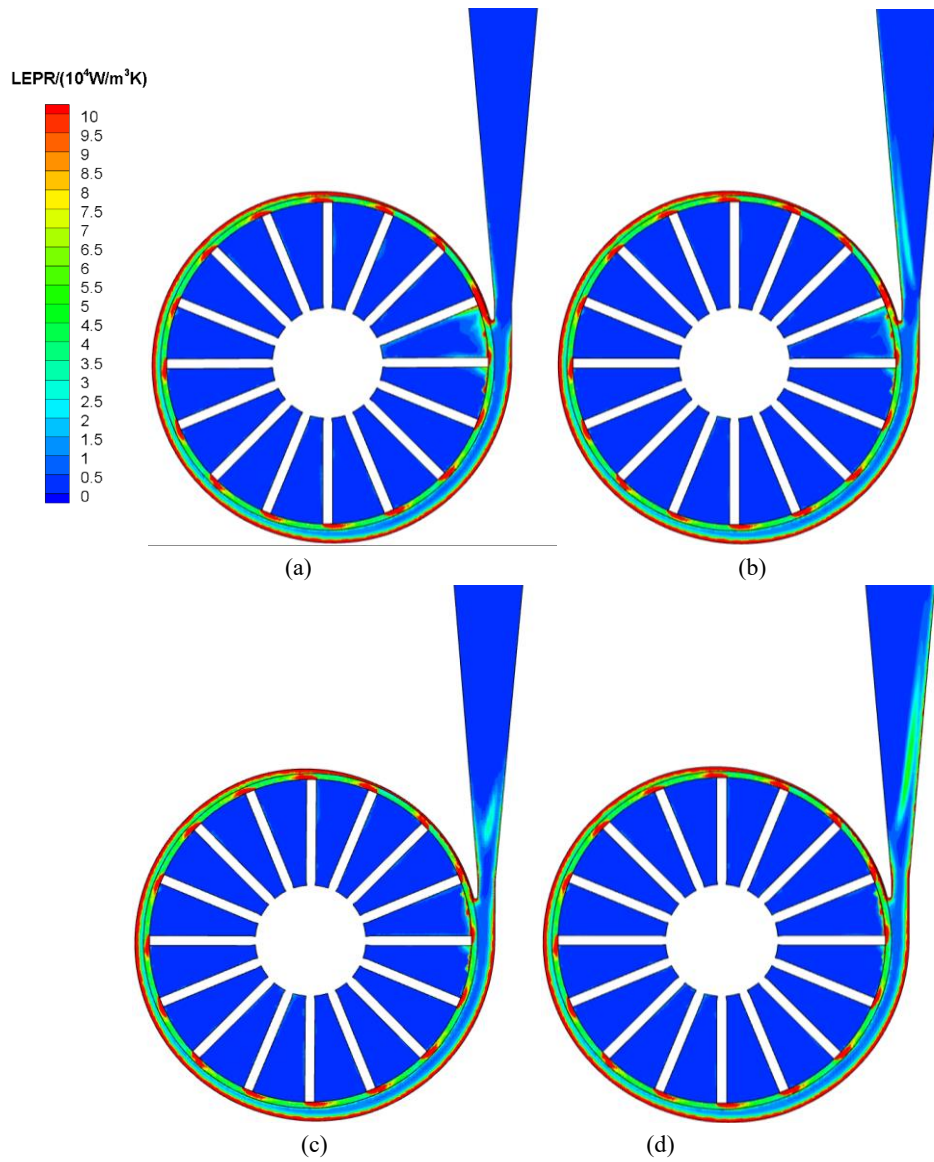


Fig. 14 (a, b, c, d). Distribution of LEPR in the central section of impeller under different flow rates at (a) $0.2 Q_d$ (b) $0.6 Q_d$ (c) $1.0 Q_d$ and (d) $1.4 Q_d$.

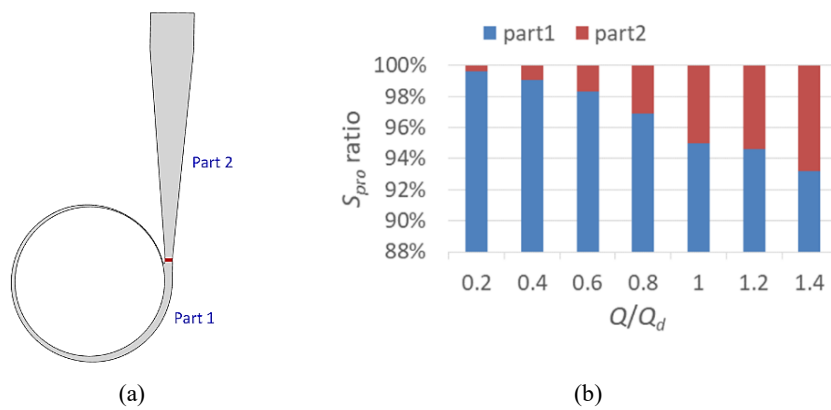


Fig. 15 (a, b). Entropy production at different parts of volute versus flow rate: (a) Diagram of different parts of the volute, (b) Percentage of S_{pro} in different parts of the volute.

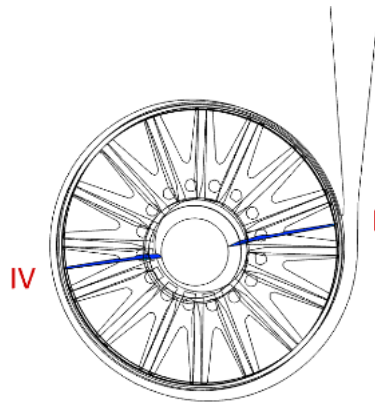


Fig. 16. Schematic of flow in channels I and IV.

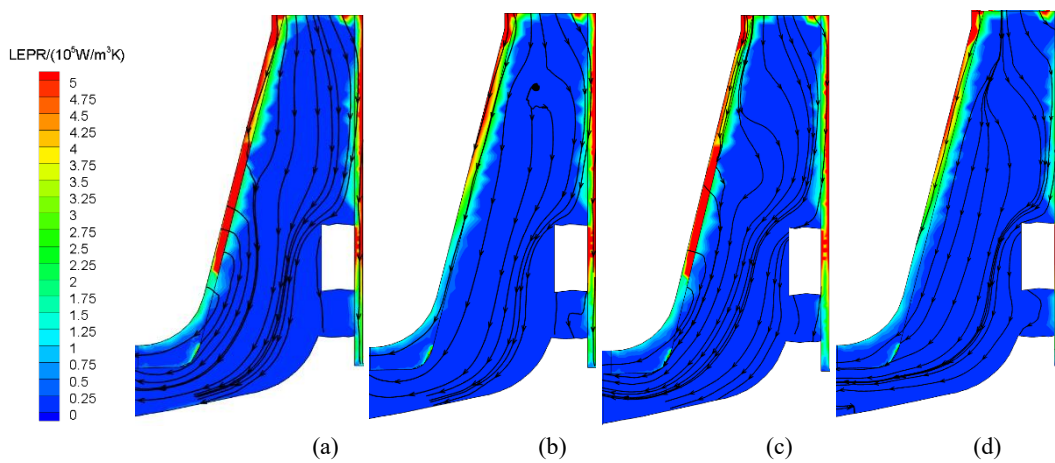


Fig. 17 (a, b, c, d). Distribution of entropy production and streamline in channel I under different flow rates at (a) $0.2 Q_d$ (b) $0.6 Q_d$ (c) $1.0 Q_d$ and (d) $1.4 Q_d$.

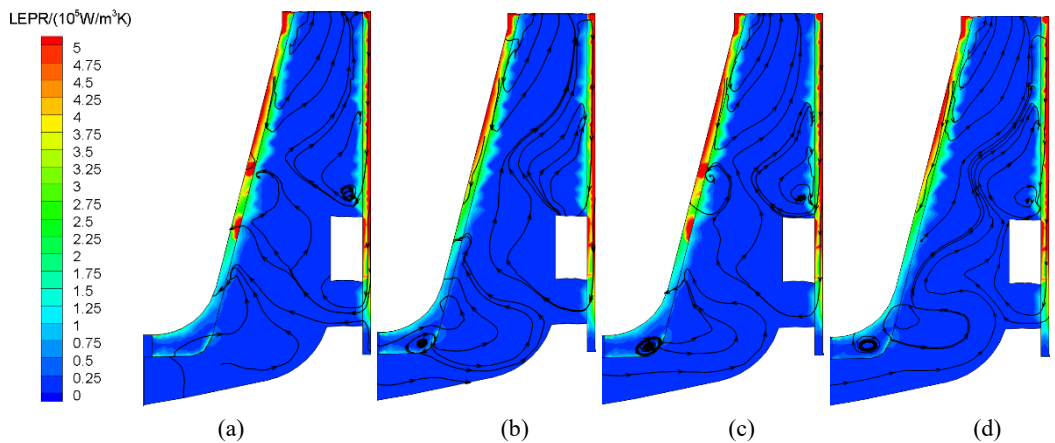


Fig. 18 (a, b, c, d). Distribution of entropy production and streamline in channel IV under different flow rates at (a) $0.2 Q_d$ (b) $0.6 Q_d$ (c) $1.0 Q_d$ and (d) $1.4 Q_d$

and they are much higher than those at the inner part of the flow channel (Figs. 17 and 18). This is due to the large velocity gradient of the fluid near the wall at high speed.

The wall friction and rotor–stator interaction between the blade and the front chamber leads to a

pressure gradient along the axial direction. Therefore, the streamline starts from the wall to the center of the channel, and the entropy production on the wall is large. The zigzag entropy production area (green region of LEPR) appears due to the flow mixing between the impeller and the front chamber. As shown in Fig. 2, the flow passage of the impeller gets

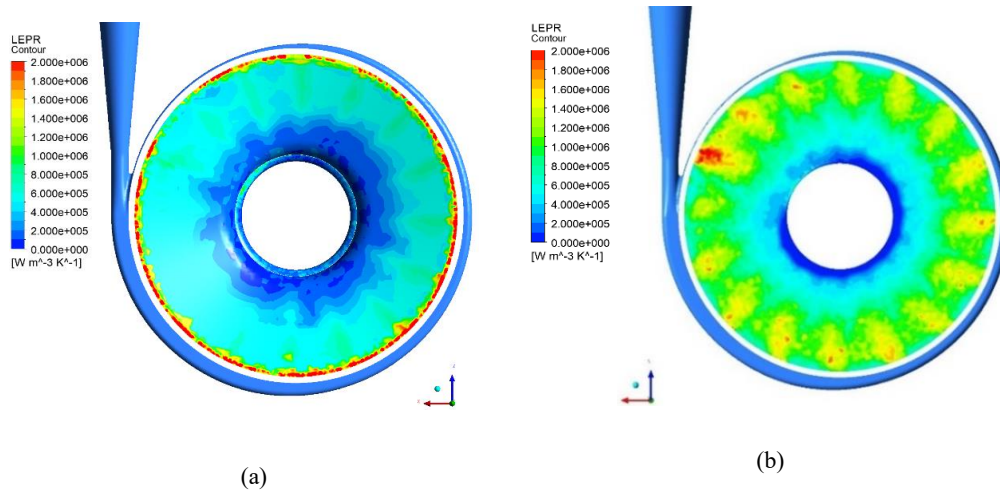


Fig. 19 (a, b). Distribution of entropy production at the outer surface of (a) front chamber and (b) back chamber under flow rate of $0.2 Q_d$.

broader along the axial direction from the front chamber to the back chamber. Owing to the larger section area of the impeller near the back chamber, the local streamline is forced along the wall of back chamber, leading to more friction loss than that in the front chamber. This can be illustrated more clearly in Fig. 19, which shows the LEPR at the outer surface of front and back chamber under flow rate of $0.2 Q_d$ (Figures under other flow rates shows the similar distribution of LEPR). The LEPR at back chamber surface is overall higher than that at the front chamber surface except for the outer edge. The results are in consistency with that in Fig. 12 that the S_{pro} value in the back chamber is higher than that in the front chamber. At the outer surface of back chamber, regions of high S_{pro} are mainly located with high radius corresponding to the special structure of the impeller, which is induced by the wake of impeller blade and its shock with the wall of the back chamber.

As shown in Fig. 10, the backflow clearly occupies channel I, which is near the volute tongue. To the blade passage far away from the volute tongue, the flow mostly passes through the passage with some vortices (Fig. 10). Numerous blades narrow the passage and limit the formation of large vortices in some channels, thus the backflow phenomenon does not worsen with the increase of flow rates. Therefore, almost the same value of high entropy production appears in the front or back chambers in regardless of the flow rates (Fig. 13).

4. SUMMARY

In this paper, the influence of the straight blade on the performance characteristics and energy loss of a high-speed pump were studied by numerical simulation. Adding straight blades in the impeller helps to raise the pump head, but it has adverse effects on pump efficiency. The energy loss represented by entropy production are mostly located at the trailing edge of the blade, the near-tongue region of the volute, and the walls of volute and front

and back chambers. The following conclusions are drawn:

- (1) Approximately 96% of the energy loss in the high-speed pump is produced in the volute, gap, and front and back chambers. Most of the flow parts are insensitive to the flow rates, except for the volute.
- (2) In the gap, the high LEPR region mainly concentrates on the region near the trailing edge of the impeller, which is consistent with the small region including pressure gradients. Large energy loss is observed in the gap at area between the volute tongue and the near-tongue passage.
- (3) In the volute, the circumferential pressure variation causes high S_{pro} at the volute wall. At low flow rates, the backflow in the diffuser give rise to more friction and energy loss. The percentage of S_{pro} in the volute increases from 0.5% to 7% when the flow rates increases from $0.2 Q_d$ to $1.4 Q_d$.
- (4) In the chambers, the wall friction and rotor–stator interaction between the blade and the front chamber lead to a pressure gradient along the axial direction. More friction loss generates in the back chamber than front.
- (5) When design a hydraulic model of high-speed pump, the cross-section area of volute, front and back chamber should be carefully calculated, and the control of passing velocity and friction loss are the key to optimization.

ACKNOWLEDGEMENTS

This work was supported by the National Nature Science Foundation of China (51706206), Key Research and Development Program of Zhejiang Province (2019C03117), Zhejiang public welfare projects (LGF19E060001), Postdoctoral Sustentation Fund (2017M622561), and Starting Foundation of Zhejiang Sci-Tech University (16022180-Y).

REFERENCES

- Alemi, H., S. A. Nourbakhsh, M. Raisee and A. F. Najafi (2015). Effects of Volute Curvature on Performance of a Low Specific-Speed Centrifugal Pump at Design and Off-Design Conditions. *Journal of Turbomachinery-Transactions of The Asme* 137(4), 041009.
- Cui, B., C. Jie, L. I. Xiaojun, L. Zhe, C. Haibing and H. Anda (2018). Experiment and Numerical Simulation of Cavitation Evolution in High Speed Centrifugal Pump with Inducer. *Transactions of the Chinese Society for Agricultural Machinery* 49(4), 148-155.
- Barrio, R., J. Parrondo and E. Blanco (2010). Numerical analysis of the unsteady flow in the near-tongue region in a volute-type centrifugal pump for different operating points. *Computers and Fluids* 39(5), 859-870.
- Chang, H., W. Shi, W. Li and J. Liu (2019). Energy loss analysis of novel self-priming pump based on the entropy production theory. *Journal of Thermal Science* 28(2), 306-318.
- Cui, B., D. Chen, C. Wang, Z. Zhu, Y. Jin and Y. Jin (2013). Research on performance of centrifugal pump with different-type open impeller. *Journal of Thermal Science* 22(6), 586-591.
- David, J. (1997). *Centrifugal Pump Design and Performance*. Conecpts ETI, Inc.
- Fang, P., J. Du and S. Yu (2020). Impeller (straight blade) design variations and their influence on the performance of a centrifugal blood pump. *The International Journal of Artificial Organs*, 0391398820913559.
- Hou, H., Y. Zhang and Z. Li (2017). A numerically research on energy loss evaluation in a centrifugal pump system based on local entropy production method. *Thermal Science* 21(3), 1287-1299.
- Jafarzadeh, B., A. Hajari, M. M. Alishahi and M. H. Akbari (2011). The flow simulation of a low-specific-speed high-speed centrifugal pump. *Applied Mathematical Modelling* 35(1), 242-249.
- Jia, X., B. Cui, Z. Zhu and X. Yu (2018). Numerical investigation of pressure distribution in a low specific speed centrifugal pump. *Journal of Thermal Science* 27(1), 25-33.
- Kock, F. and H. Herwig (2004). Local entropy production in turbulent shear flows: a high-Reynolds number model with wall functions. *International journal of heat and mass transfer* 47(10-11), 2205-2215.
- Li, D., H. Wang, Y. Qin, L. Han, X. Wei and D. Qin (2017). Entropy production analysis of hysteresis characteristic of a pump-turbine model. *Energy Conversion and Management* 149, 175-191.
- Li, Y., S. Yuan and H. Lai (2017). Numerical study of unsteady flows with cavitation in a high-speed micro centrifugal pump. *Journal of Thermal Science* 26(1), 18-24.
- Mathieu, J. and J. Scott (2000). *An introduction to turbulent flow*: Cambridge University Press.
- Pei, J., F. Meng, Y. Li, S. Yuan and J. Chen (2016). Effects of distance between impeller and guide vane on losses in a low head pump by entropy production analysis. *Advances in Mechanical Engineering* 8(11), 8/11/1687814016679568.
- Song, G., L. P. Chua and T. M. Lim (2010). Numerical study of a centrifugal blood pump with different impeller profiles. *Asaio Journal*, 56(1), 24-29.
- Su, X., S. Huang, X. Zhang and S. Yang (2016). Numerical research on unsteady flow rate characteristics of pump as turbine. *Renewable Energy* 94, 488-495.
- Su, X., Z. Tang, Y. Li, Z. Zhu, K. Mianowicz and P. Balaz (2020). Research of Particle Motion in a Two-Stage Slurry Transport Pump for Deep-Ocean Mining by the CFD-DEM Method. *Energies* 13(24).
- Wang, C., Y. Zhang, H. Hou, J. Zhang and C. Xu (2019). Entropy production diagnostic analysis of energy consumption for cavitation flow in a two-stage LNG cryogenic submerged pump. *International Journal of Heat and Mass Transfer* 129, 342-356.
- Yang, B., B. Li, H. Chen and Z. Liu (2019). Entropy production analysis for the clocking effect between inducer and impeller in a high-speed centrifugal pump. *ARCHIVE Proceedings of the Institution of Mechanical Engineers Part C Journal of Mechanical Engineering Science* 1989-1996 (vols 203-210).
- Yuan, S., J. Zhang, Y. Tang, J. Yuan and Y. Fu (2009). *Research on the design method of the centrifugal pump with splitter blades*. Paper presented at the Fluids Engineering Division Summer Meeting.
- Yuan, Y. and S. Yuan (2017). Analyzing the effects of splitter blade on the performance characteristics for a high-speed centrifugal pump. *Advances in Mechanical Engineering* 9(12), 1687814017745251.